# ResearchOnline@JCU



This is the author-created version of the following work:

Prajapati, Megha, Ravi Kant, Chhaya, Hussain, Aasim, and Jacob, Mohan V. (2024) Hierarchical NiCo-LDH layered composite on PANI coated Ni foam for highly efficient supercapattery applications. New Journal of Chemistry, 48 pp. 18376-18391.

Access to this file is available from:

https://researchonline.jcu.edu.au/85370/

© The Royal Society of Chemistry and the Centre National de la Recherche Scientifique 2024.

Please refer to the original source for the final version of this work:

https://doi.org/10.1039/D4NJ03345K

# Hierarchical NiCo-LDH Layered Composite on PANI coated Ni Foam for Highly Efficient Supercapattery Applications

Megha Prajapati<sup>a,b</sup>, Chhaya Ravi Kant<sup>a\*</sup>, Aasim Hussain<sup>c</sup>, Mohan V. Jacob<sup>b</sup>

<sup>a</sup>Department of Applied Sciences and Humanities, Indira Gandhi Delhi Technical University for Women, Delhi 110006, India

<sup>b</sup>Electronics Materials Lab, College of Science and Engineering, James Cook University, Townsville, QLD 4811, Australia

<sup>c</sup> Department of Physics, Jamia Millia Islamia, New Delhi 110025, India

\*Corresponding Author-chhayaravikant@igdtuw.ac.in

### **Abstract**

Supercapatteries combine the high-power density characteristic of supercapacitors with the high energy density typically found in batteries, offering a promising solution for advanced energy storage applications. We present an efficient two-step method to fabricate hierarchical, binder-free NiCo layered double hydroxide (LDH) nanosheet arrays supported on polyaniline layered nickel foam (NF). PANI@NiCo-LDH/NF nanocomposite serves as the anode in the supercapattery, leveraging the high capacitance and improved conductivity of the combined materials, yielding a significantly high specific capacity of 1481 C/g (3703.33 F/g). Coffee grounds derived reduced graphene oxide (rGO), providing a sustainable and environmentally friendly material with excellent electrical conductivity and high mechanical strength, serves as the cathode. The synergy between the PANI@NiCo-LDH/NF anode and the rGO cathode creates a novel and highly efficient supercapattery system. The fabricated supercapattery device offers an energy density of 54.44 Wh/kg at a power density of 0.702 kW/kg and exhibits good cyclability with capacitance retention of 84.88% and Coulombic efficiency of 77.68% over 5000 charging/discharging cycles. This innovative approach addresses the limitations of traditional energy storage devices, paving the way for more versatile and sustainable energy solutions.

Keywords: NiCo layered double hydroxide (LDH); Electrodeposition; PANI; Metal-Organic Frameworks (MOFs); Energy Storage Devices; Supercapattery

#### 1. Introduction

The relentless increase in pollution levels driven by the widespread use of fossil fuels and the surge in industrial activities has intensified the need for sustainable and eco-friendly energy solutions [1]. The detrimental impact of conventional energy sources on the environment necessitates a shift towards renewable energy technologies such as solar, wind, and hydroelectric power. While promising, these renewable sources present a significant challenge: their intermittent nature requires efficient and reliable energy storage systems to ensure a stable and continuous power supply. Consequently, the advancement of sophisticated energy storage devices has become a pivotal area of research. Traditional batteries, such as lithium-ion batteries, have been the cornerstone of energy storage for decades. Because of their high energy density, they are apt for applications requiring long-term energy storage. However, batteries are often limited by their relatively shorter cycle life, slow charge and discharge rates, and

safety hazards [2]. These limitations hinder their ability to meet the growing demands of modern energy systems, particularly in applications requiring rapid energy delivery and frequent cycling. Whereas, supercapacitors outshine in delivering high power density with fast charging-discharging process, making them suitable for applications that demand quick bursts of energy [3]–[5]. Supercapacitors can be charged and discharged in a matter of seconds, and they boast a long cycle life, often exceeding hundreds of thousands of cycles. Despite these advantages, supercapacitors suffer a major drawback: their energy density is significantly lower than that of batteries, limiting their use in applications requiring sustained energy delivery. To address the limitations of both batteries and supercapacitors, hybrid energy storage devices known as supercapatteries have emerged. Supercapatteries are designed to combine high-power density and remarkable cyclability of supercapacitors with high-energy density of batteries. With this hybrid approach aims to create an energy storage solution that can meet the demands of both high-power and high-energy applications, providing a more versatile and efficient alternative to traditional storage devices [6], [7].

The development of supercapatteries is focused on exploring advanced materials to enhance performance, with metal-organic frameworks (MOFs) receive significant attention as potential electrode materials. MOFs exhibit unique morphologies, high porosity, large surface areas (≈2000–8000 m²/g), structural uniformity, and tuneable functionality. These properties are achieved by combining metal ions (e.g., Zn<sup>2+</sup>, Cu<sup>2+</sup>, Ni<sup>2+</sup>) with multidentate organic linkers (e.g., carboxylic acids, bipyridine). MOFs offer several advantages for supercapattery applications, such as intrinsic redox-active sites and remarkable storage capacity due to their high surface area [8]. They also enhance gas storage [9], catalysis, sensors [10], drug delivery [11], and electrochemical energy storage performance [12], [13]. In context of supercapattery, MOFs can also be derived into transition metal oxides/hydroxides/phosphides/sulphides, particularly those based on nickel (Ni) and cobalt (Co), have shown significant promise due to their excellent electrochemical properties. Nickel-cobalt MOFs (NiCo MOFs) and their derivatives, such as NiCo-LDH, have substantially improved capacitance and cycling stability, making them promising candidates for hybrid energy storage devices [14][15]. In this context, the 2-methylimidazole (2-MIM) linker is recognized as a promising candidate for LDH synthesis, functioning as a surfactant and weak base ( $pK_a = 7.86$ ) that gradually releases hydroxide ions during the reaction. This controlled release of metal cations from the initial MIM-metal complex, alongside hydroxide ions, facilitates the growth of ultrathin NiCo-LDH nanosheets, resulting in a 3D porous hierarchical nanostructure [16]–[19].

The layered structure of NiCo-LDH allows for efficient ion intercalation and deintercalation, which is crucial for high-performance energy storage. Recent advancements have led to nanocomposites derived from MOFs, making them suitable as cathodes, anodes, matrices, and precursors in energy storage devices. LDH has a typical formula of  $[M^{III}_xM^{II}_{1-x}(OH)_2]^{x+}[N^{n-x/n}]^{x-}$ . mH<sub>2</sub>O, where  $M^{III}$  and  $M^{II}$  are trivalent and divalent metal cations and form octahedral host layers that resemble brucite. On the other hand,  $N^{n-}$  stands for charge-balancing anions found in the LDH interlayers, such as  $NO_3^{2-}$ ,  $CO_3^{2-}$ , and water molecules. The properties of the laminar structure and flexible exchange of anions in LDH structure typically favour the ion transport throughout the charging/discharging process [19]–[21]. Furthermore, hydrophilic properties of LDH structures are extremely beneficial for ion transport in aqueous electrolyte. However, nanocomposites derived from MOFs face challenges such as relatively low electrical conductivity and stability under electrochemical conditions. Addressing these issues is

essential for their practical applications in hybrid energy storage devices. To overcome this issue, researchers have explored the incorporation of conductive polymers, such as polyaniline (PANI), into the composite material. PANI is a conducting polymer known for its high conductivity, and ease of synthesis, and good environmental stability. When integrated into a NiCo-LDH matrix, PANI can enhance the overall conductivity of the composite, providing a more efficient pathway for electron transport. Additionally, PANI contributes to the pseudocapacitance of the composite, further boosting its energy storage capacity. By synergistically combining advanced materials, researchers can create supercapatteries that meet the growing demands of modern energy systems while contributing to environmental sustainability [22]. For instances, Hu et al. [23] synthesised NiCo LDH@PANI nanocomposite on carbon cloth (CC). The surface of carbon cloth (CC) is first electrodeposited with a PANI layer to cover it uniformly. Next, through a hydrothermal procedure, NiCo-LDH nano scrolls were synthesised. The specific capacity of NiCo-LDH@PANI@CC nanocomposite was found to be 901 C/g (1 A/g) [23]. Also, Pan et al. [24] synthesised NiCo<sub>2</sub>O<sub>4</sub>@PANI nanotubes anchored on carbon textiles via facile hydrothermal process and followed by electrodeposition method. The NiCo<sub>2</sub>O<sub>4</sub>@PANI composite electrodes show improved specific capacity of 720.4 C/g (1 A/g) compared with NiCo<sub>2</sub>O<sub>4</sub> (663.6 C/g) because of the benefits its hollow heterostructure and binder-free nature [24]. However, there is still a room for enhancement in performance and optimization of the structural properties.

Herein, encouraged by the ideas mentioned above, we report an effective two step approach to fabricate hierarchical binder-free NiCo LDH nanosheet arrays supported on polyaniline layer (PANI@NiCo LDH/NF). The fabrication process begins with the electrodeposition of PANI on a nickel foam substrate. This is followed by direct growth of NiCo-LDH on the PANI-coated nickel foam through a solvothermal process. This method ensures a strong adhesion between the NiCo-LDH and the conductive PANI matrix, resulting in a composite material with enhanced electrochemical properties. The PANI/NiCo-LDH nanocomposite serves as the anode in the supercapattery, leveraging the high capacitance and improved conductivity of the combined materials. As a result, specific capacity of the PANI@NiCo LDH/NF was found to be 1481 C/g (3703.33 F/g).

On the cathode side, carbon-based materials, particularly graphene and its derivatives, have been extensively studied to improve the performance of supercapatteries. rGO offers excellent electrical conductivity, high mechanical strength with elevated surface area, making it a viable candidate for energy storage [7]. However, the production of graphene-based materials can be expensive and environmentally taxing. Researchers have explored using sustainable and costeffective sources for graphene production to address this. One such source is coffee grounds, a standard waste product from the coffee industry. Coffee grounds which are reduced to rGO, provide a sustainable and environmentally friendly material for energy storage devices. The synergy between PANI@NiCo-LDH/NF anode and rGO (derived from coffee grounds) cathode creates a novel and highly efficient supercapattery system. As a result, the supercapattery device comprising PANI@NiCo LDH and rGO demonstrates an energy density of 54.44 Wh/kg and a power density of 0.702 kW/kg. Moreover, the device shows excellent cyclability, maintaining a Coulombic efficiency of 77.68% and a capacitance retention of 84.88% over 5000 charge-discharge cycles. The advantages of high capacitance, improved conductivity, and mechanical strength lead to a supercapattery that can deliver high electrochemical performance. This innovative approach addresses the limitations of traditional

energy storage devices and paves the way for more versatile and sustainable energy solutions. Researchers continue to explore these materials to unlock their full potential, aiming to develop next-generation energy storage devices that meet the increasing demands of contemporary energy systems.

# 2. Experimental section

#### 2.1. Materials

Raw products including potassium hydroxide (KOH, 98 %), sulfuric acid (H<sub>2</sub>SO<sub>4</sub>, 98%), methanol (CH<sub>3</sub>OH, AR 99 %), N-methyl-2-pyrrolidone (NMP, AR 98 %), ethanol (CH<sub>3</sub>CH<sub>2</sub>OH, AR 99 %), and deionised (DI) were supplied from SRL. 2-methylimidazole (2-MIM, C<sub>4</sub>H<sub>6</sub>N<sub>2</sub>, AR 99 %), Aniline (C<sub>6</sub>H<sub>7</sub>N, 98%), nickel nitrate hexahydrate (Ni(NO<sub>3</sub>)<sub>2</sub>.6H<sub>2</sub>O), polyvinylidene fluoride (PVDF, 98 %), and cobalt nitrate hexahydrate (Co(NO<sub>3</sub>)<sub>2</sub>.6H<sub>2</sub>O) were received from Sigma-Aldrich. Nickel Foam (NF) was supplied by Nanoshel (India). All reagents were utilised as received from the manufacturer and were not further purified.

# 2.2. Samples synthesis

# 2.2.1. Synthesis of PANI Functionalized NF (PANI/NF)

The preparation of PANI/NF is depicted in Figure 1 (step I). The polyaniline layer was electrodeposited onto the NF surface employing cyclic voltammetry (CV) technique in three-electrode cell configuration utilising Ag/AgCl reference electrode (RE), NF (1 x 4 cm<sup>2</sup>) as working electrode (WE), and Platinum (Pt) mesh counter electrode (CE). Aqueous solution of 1 M  $_{2}$ SO<sub>4</sub> and 0.1 M aniline was utilised as electrolyte, and ten cycles were conducted within a voltage range of -0.2 to 0.8 V at 100 mV/sec. After that, PANI/NF was rinsed thoroughly with DI and dried at 60°C for 5 hrs. The mass of the PANI on NF was found to be 0.2  $\pm$  0.1 mg.

# 2.2.2. Synthesis of PANI-mediated NiCo LDH nanoarray on NF (PANI@NiCo LDH/NF) as anode

The preparation of PANI@NiCo LDH/NF is demonstrated in Figure 1 (step II). Ni(NO<sub>3</sub>)<sub>2</sub>·6H<sub>2</sub>O (10 mmol), 2-MIM (40 mmol), and Co(NO<sub>3</sub>)<sub>2</sub>·6H<sub>2</sub>O (10 mmol) were dissolved into 50 mL methanol and stirred vigorously until reagents dissolved completely. Afterwards, the precursor mixture along with PANI/NF was transferred in autoclave and maintained at 120 °C for 15 hrs. Following cooling, the PANI@NiCo LDH/NF was taken out, washed repeatedly with methanol, and subsequently vacuum-dried at 60°C for 10 hours. The mass of PANI@NiCo LDH on NF was found to be  $1.4 \pm 0.2$  mg. Additionally, for comparison, NiCo LDH/NF was synthesised directly under same condition without electrodeposition of PANI. The mass of NiCo LDH on NF was found to be  $1.1 \pm 0.2$  mg.



Figure 1. Systematic depiction of the preparation process of PANI@NiCo LDH/NF sample

# 2.2.3. Preparation of rGO derived from coffee grounds as cathode

The synthesis technique rGO was taken from the reference [7]. Coffee grounds were employed as raw material, microwave pyrolysis was employed as a thermal conversion method, and ferric chloride (FeCl<sub>3</sub>) was used as a chemical post-treatment. Initially, 10 g of coffee grounds was cleaned with DI and ethanol until it becomes free from contaminants. Afterwards, it was dried for one hour at 110 °C and then pyrolyzed for thirty minutes at 1 kW with 4 m/L N<sub>2</sub> flow. Following, resulted material was processed for 24 hours at room temperature using FeCl<sub>3</sub> at a weight ratio of 1:1. The material was then repeatedly cleaned with DI and dried for an hour at 110 °C. The resulting material was again pyrolyzed for 30 minutes@1 kW. Afterwards, GO was reduced to rGO at 500 °C for 5 hours (in tubular furnace) with an Ar environment. Further, using NMP as the solvent, a mixed slurry of PVDF, and rGO powder in the ratio of 2:8 was prepared and drop cast onto the cleaned NF piece. At last, the electrodes were dried for ten hours at 60° C. The mass loading on rGO was found to be 1.7 ± 0.1 mg/cm<sup>2</sup>.

#### 2.3. Sample Characterization

The samples' structural morphology and surface characteristics were analysed using a Nova Nano field emission scanning electron microscope (FESEM 450 by FEI). The gold coating was done on samples, before performing the SEM analysis. Transmission Electron Microscopy (TEM, FEI, Electron Optics, Tecnai 200 kV) was utilized to inspect the internal and detailed structure of the synthesized samples. Further, for TEM analysis, sample were dispersed in ethanol, and ultrasonicated for 45 minutes. Afterwards, the sample was drop-casted over the carbon coated copper grids of 200 Mesh. Fourier-transform infrared (FT-IR) spectrometer (Shimadzu, Japan) was employed to determine the functional and chemical composition within the 500 to 4000 cm<sup>-1</sup> range. Also, FTIR spectrum was recorded at a standard resolution of 4 cm<sup>1</sup>, with 30 scans for better accuracy. The material's specific surface area and porosity were examined using the Brunauer-Emmett-Teller (BET) technique with a Nova Touch Quantachrome by LX2 (under N<sub>2</sub> flow). Also, for BET, the samples were degassed at 200°C for hours.

Additionally, X-ray photoelectron spectroscopy (XPS) investigations was carried out with a Thermo Fisher Scientific micro-focused X-ray system (72 W, 12000 V, 400 nm spot size) monochromatic Al-K $\alpha$  source (hv = 1486.6 eV), with a hemispherical analyser, and a 128-

channel plate detector, with flood gun (Ar ions) to reduce to charge shift. The calibration of the XPS was done through the carbon peak of the material. Cu  $K\alpha$  radiation Bruker D8 Advance X-ray diffractometer was used to collect X-ray diffraction (XRD) data.

#### 2.4. Electrochemical measurements

Electrochemical properties were examined using Autolab Potentiostat (USA) electrochemical workstation in three-cell system with Pt mesh as RE, Ag/AgCl as CE, and samples on NF as WE in 1 M KOH electrolyte solution. CV was performed within the potential range of 0.5 V vs. Ag/AgCl at different sweep rates. Galvanostatic charge-discharge (GCD) measurements were investigated in a voltage window of 0.4 V, and electrochemical impedance spectroscopy (EIS) study was conducted in frequency ranges from 10 mHz to 0.1 MHz at open circuit voltage.

Specific capacity (C, C/g) and capacitance (C<sub>s</sub>, F/g) of the electrodes was estimated via measured GCD plots given as equation (1), and (2) respectively.

$$C = \frac{\Delta txI}{m} \tag{1}$$

$$C_{s} = \frac{\Delta t \times I}{m \times \Delta V} \tag{2}$$

 $\Delta t$  (sec) represents discharging time, I (A) denote applied current, m (g) stands for the active mass of the electrode, and  $\Delta V$  (V) indicates the voltage window.

# 2.5. Assembly of PANI@NiCo LDH/NF//rGO supercapattery device

Supercapattery device was designed by coupling two electrodes of distinct nature i.e., PANI@NiCo LDH/NF as battery grade and rGO as capacitive electrode. A sheet of Whatman filter paper dipped in 1 M KOH electrolyte was positioned between both electrodes in order to prevent short circuit while electrochemical process. In order to balance the charges on both electrodes, the mass ratio of the negative electrode (rGO) (-) to the positive electrode (PANI@NiCo LDH/NF) (+) was optimized using mass balancing equation (3) given below:

$$\frac{\mathbf{m}^{-}}{\mathbf{m}^{+}} = \frac{\mathbf{C}_{S}^{+} \mathbf{x} \Delta \mathbf{V}^{+}}{\mathbf{C}_{S}^{-} \mathbf{x} \Delta \mathbf{V}^{-}} \tag{3}$$

The value of specific capacitance  $(C_s, F/g)$  was determined using equation (4)

$$C_{s} = \frac{\Delta t x I}{M x \Delta V} \tag{4}$$

Here, M denoted active mass of the electrodes

The energy density (Wh/kg) and power density (kW/kg) were estimated using the following equations (5, and 6) respectively:

$$E_{\rm S} = \frac{C_{\rm S} x \Delta V^2}{2x3.6} \tag{5}$$

$$P_{s} = \frac{Ex3600}{\Delta t} \tag{6}$$

### 3. Reaction Mechanism

The synthesis of PANI@NiCo LDH on NF was performed employing electrodeposition followed by solvothermal technique. Firstly, PANI layer was grown directly on the surface of NF via electrodeposition method that only required aniline monomer and protonic acids (here, H<sub>2</sub>SO<sub>4</sub>) as an electrolyte [25]–[27]. The electro-polarization of PANI in aqueous solution is accredited on redox reactions occur on the surface of the NF that acts as working electrode (WE) along with the counter and reference electrodes, are dipped in the electrolyte, and subjected to an applied potential. Electrochemical oxidation of the aniline facilitates polymerization at the electrode surface, leading to polyaniline film deposition in a process known as chemical oxidative polymerization, which can be explained in steps below:

Initially, aniline monomers are oxidized at the anode in the presence of an acidic electrolyte and, this process generates radical cations (aniline radical cations) (equation (7)).

$$C_6H_5NH_2 \rightarrow C_6H_5NH_2^{\bullet+} \tag{7}$$

These radical cations pair with other radical cations or monomers of aniline, leading to dimers and higher oligomers. The aniline radical cation carries a positive charge, making the paraposition (p-position) highly electronegative. As a result, coupling typically occurs at the p-position relative to the amino group [28].

$$C_6H_5NH_2^{\bullet+} + C_6H_5NH_2 \rightarrow (C_6H_5NH_2^{\bullet+})_2$$
 (8)

This process progresses, resulting in the formation of longer oligomers and eventually forming polyaniline chains. Finally, the growth of the polymer film is regulated or terminated by various factors, including the applied potential, availability of monomers, and the nature of the electrolyte used in the reaction [27][29]. Thereafter, PANI/NF along with solution containing Ni(NO<sub>3</sub>)<sub>2</sub>·6H<sub>2</sub>O, 2-MIM, and Co(NO<sub>3</sub>)<sub>2</sub>·6H<sub>2</sub>O, and solvothermal reaction was carried out, where both Co and Ni ions were coordinated with four imidazolates (organic linker) (C<sub>4</sub>H<sub>6</sub>N<sub>2</sub>) into a tetrahedral framework on the surface of the PANI/NF, resulting in a hierarchical composite structure (equation 9) [30], [31][19]. Reaction mechanism of the formation of NiCo LDH is as shown below: -

$$xNi^{2+} + (1-x)Co^{2+} + 2OH^{-} \rightarrow (Ni_{x}Co_{1-x})(OH)^{+2}$$
 (9)

As, 2-MIM linker functions as a weak base and surfactant in this process, releasing hydroxide ions gradually over time [19].

The nitrogen species from the PANI structural units serve as bridging points, offering a strong coupling effect that facilitates direct growth of the NiCo LDH.

# 4. Results and discussion

Figure 2 demonstrated SEM micrographs of nickel foam (NF), PANI/NF, and PANI@NiCo LDH/NF. The surface of the NF (Figure 2a) underwent a noticeable transformation following the electro-polymerization of PANI (Figure 2b). The NF surface becomes rough due to uniform distribution of well-coated conductive layer of PANI. Furthermore, the globular sponge-like structures of PANI dispersed evenly across the surface giving its coarse texture [22][32]. After the solvothermal process, homogeneous layer of NiCo LDH hierarchical porous structure completely covers the PANI/NF's surface (Figure 2c, d). The existence of imino groups in PANI/NF layer offer abundant active sites, increase the mass transfer, enhances the binding

force between NF and LDH nanosheets. As can be seen in enlarged FESEM micrograph (Figure 2c, d), NiCo LDH/NF nanosheets were distributed uniformly on PANI/NF's surface to form 3D hierarchal nanonetwork having size up to 400 nm (estimated from imagej software). These nanonetwork act as reservoirs for electrolyte ions, shorten their distance of transport to the surface's active sites, thereby facilitating rapid ions transport within the material matrix [33]. Furthermore, the PANI@NiCo LDH/NF nanostructure is favoured for active sites' accessibility, and direct growth on nickel foam prevents the risk of "dead mass" which makes the technique beneficial for improvements in specific capacitance with rapid kinetics for redox reactions.

Also, the SEM micrographs of NiCo LDH self-assembled directly on the NF without undergoing the PANI electro-polymerization is illustrated in Figure S1 of supplementary file. It was found that the NiCo LDH have similar morphology to that of PANI@NiCo LDH, demonstrating presence of PANI could provide the conductive channel without altering the morphology of NiCo LDH structure.

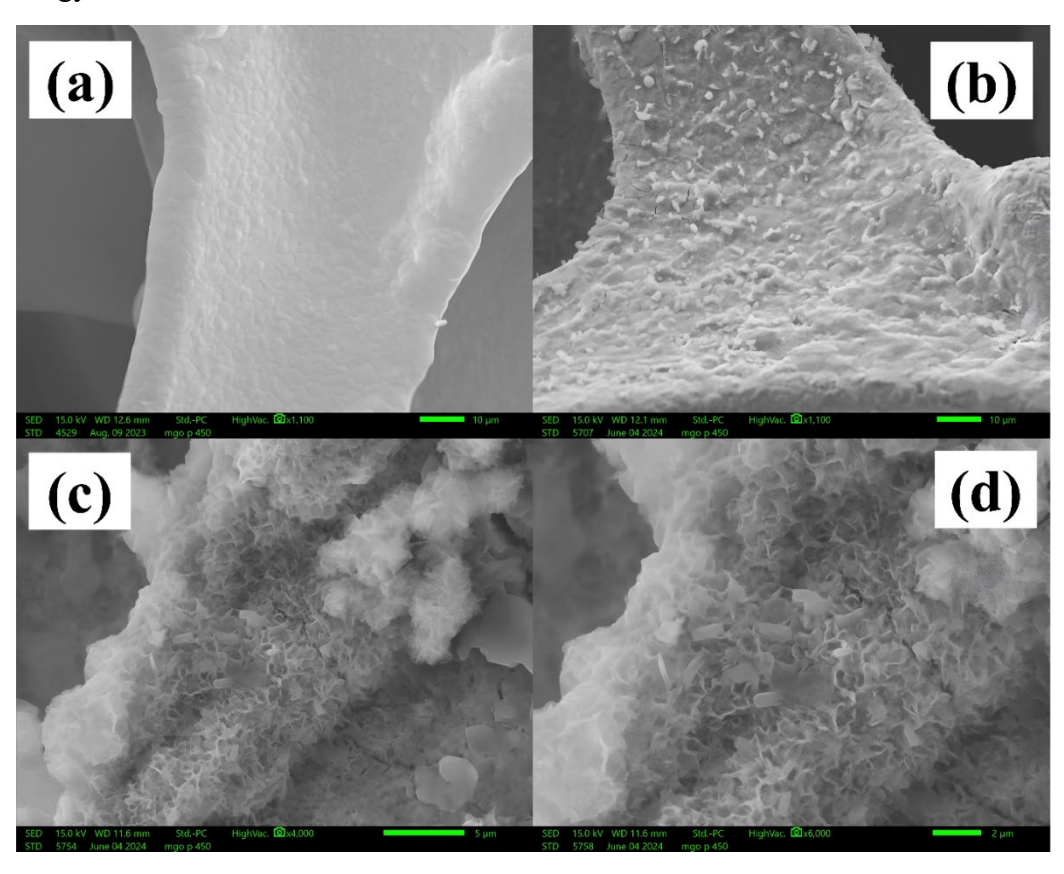


Figure 2. SEM micrographs (a). Bare NF (b). PANI electrodeposited NF (c, d). Solvothermal deposited NiCo LDH on PANI/NF

TEM provided additional insight into the structural and compositional characteristics of PANI@NiCo LDH/NF sample. PANI@NiCo LDH form a 3D hollow and hierarchical wrinkled nanosheets (~7 nm) interconnected to each other as illustrated in Figure 3 (a-c). The thin sheets and porous architecture of NiCo LDH (Figure 3d) facilitates the movement of electrolytic ions into the inner areas of the electrode material, thereby boosting the availability of electrochemically active sites and accelerating reaction kinetics. Additionally, it was noted that the NiCo LDH samples exhibit a densely stacked nanostructure with minimal aggregation. The selected area electron diffraction (SAED) pattern (inset in Figure 3d) reveals diffraction

rings for NiCo-LDH, indicating the mixture of crystalline and amorphous nature of the LDH structure. Clearly, the lattice spacings of 0.24 and 0.15 nm correspond to the (015) and (110) planes of the PANI@NiCo LDH/NF sample [34][19]. This configuration creates substantial interlayer spacing, enabling efficient utilization of active sites and providing ample buffer space while phase transformations.

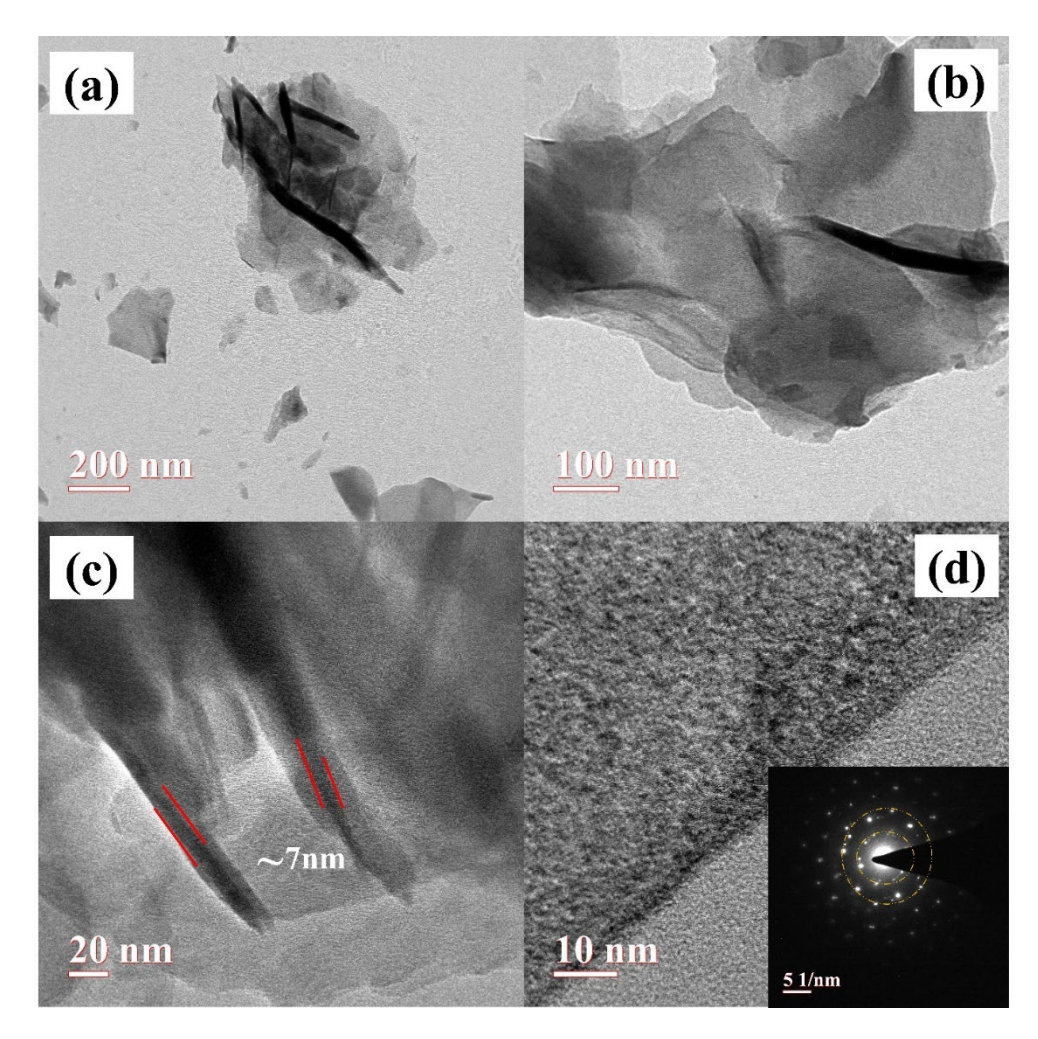


Figure 3. TEM images of PANI@NiCo LDH/NF sample

FTIR was used for finding the functional groups of the as-synthesised samples, as illustrated in Figure 4. The distinct peaks at 1289 cm<sup>-1</sup> and 1572 cm<sup>-1</sup> are ascribed to stretching vibrations of benzenoid ring (N–B–N), and quinoid ring (N = Q = N) respectively in the PANI/NF sample [22]. The FTIR spectrum of NiCo LDH/NF resembles PANI@ NiCo LDH/NF. The peak at 3625 cm<sup>-1</sup> is associated to the OH groups and H<sub>2</sub>O molecule present at the interlayer of LDH structure to counterbalance the positively charged Co and Ni. Furthermore, the existence of OH groups can effectively increase the electrode material's wettability and enhance the electrolyte ions' mobility. Furthermore, the peak1365 cm<sup>-1</sup> is associated with asymmetric stretching of carbonate ions exist in LDH interlayers [19]. .. The peaks at 673 and 510 cm<sup>-1</sup> are because of the vibration of M–O, and M–O–M (M= Co and Ni). The peak at 1097 cm<sup>-1</sup> is accredited to the v<sub>C</sub>-O and v<sub>C</sub>-H vibration bands of methanol molecules. Usually, DI (water molecules) are utilised in the synthesis process that occupy the gap between the LDH interlayers. Here, methanol's more bigger molecule size (0.44 nm) in comparison to water's

(0.28 nm) could increase the interlayer gap, which will facilitate electrolyte ion penetration during the electrical charge storage process [19][35].

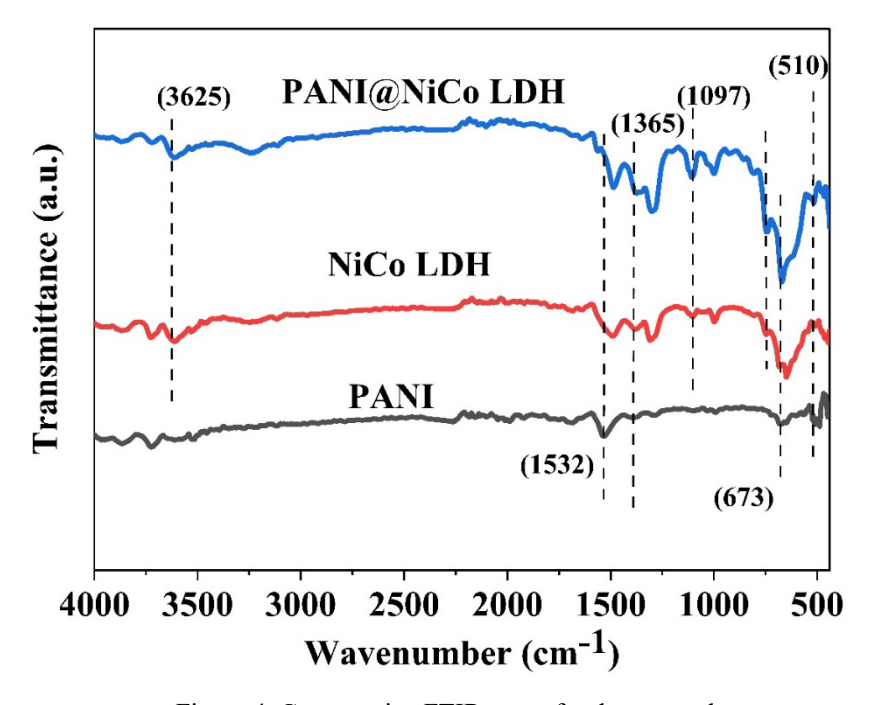


Figure 4. Comparative FTIR curve for three samples

Further, to achieve superior electrochemical performance, it is essential for the material to possess an optimal pore size distribution and a high specific surface area [36]. BET, an experimental method relies on gas physisorption into the surfaces of solid, helps to determine pore size distribution, pore volume, and specific surface area of the synthesised samples from the adsorbed monolayer gas volume. The comparative BET curve for PANI/NF, NiCo LDH/NF, and PANI@NiCo LDH/NF nanocomposites demonstrated a H2 hysteresis loop (Figure 5a) (Type IV isotherm), highlights the mesoporous characteristics of synthesised materials. The interaction between sorbent mesopore surface and gas molecules results into capillary condensation. Whereas, in mesopore-resulted capillary condensation, path of desorption and adsorption are diverse, that leads to the development of several kinds of hysteresis loops [12]. It is noticeable that that the specific surface area (SSA) of PANI@ NiCo LDH/NF is lower than those of NiCo LDH/NF i.e., 37.551 m<sup>2</sup>/g and 47.633 m<sup>2</sup>/g respectively as shown in Figure 5a. This may be explained by PANI's partial occlusion of pores, which lowers the overall pore volume. PANI consists of ample quinone nitrogen atoms in the chains of polymer which chelate redox active metal ions (Ni<sup>2+</sup> and Co<sup>2+</sup> ions of NiCo LDH) that promotes adhesion between NiCo LDH and PANI layer. As a result, PANI accesses the surface of NiCo LDH thereby functionalizes the exterior as well as interior of the material, result in reduction in surface area of PANI@ NiCo LDH/NF sample [37]. Additionally, the synthesised samples' pore size distribution, as seen in Figure 5b, demonstrated that utmost of pore diameter centred around 2.8 nm, indicating the presence of numerous mesopores that may serve as pathways for ion transport.

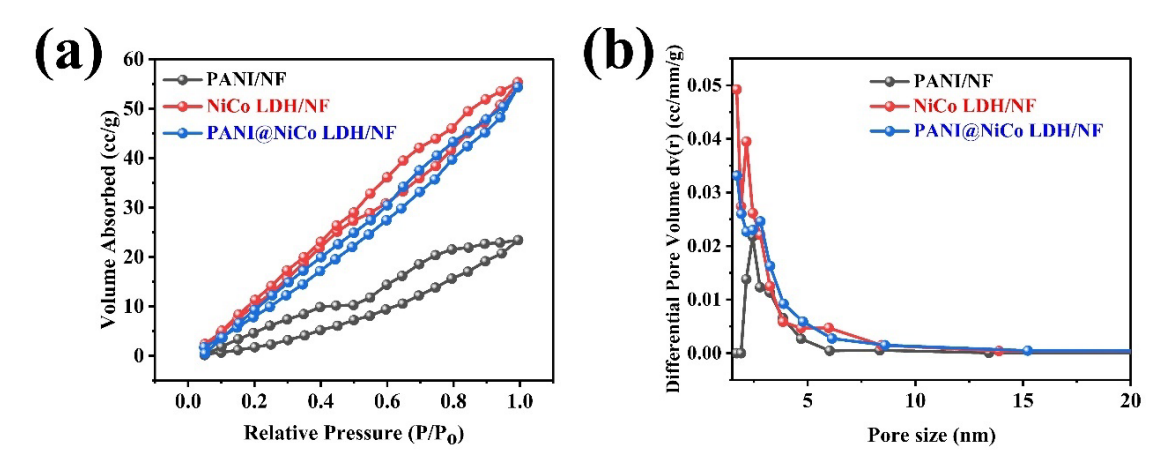


Figure 5. Comparative (a). N<sub>2</sub> adsorption-desorption isotherms (b). Pore size distribution curve for PANI/NF, NiCo LDH/NF, and PANI@NiCo LDH samples

The crystal structure of the synthesized LDH samples was determined using XRD, as depicted in Figure S2 of the supplementary datasheet. The prominent peaks at 44.3°, 51°, and 76° are attributed to the nickel foam. However, no additional signals are detected in the PANI/NF, NiCo LDH/NF, and PANI@NiCo LDH/NF samples, likely because the strong intensity of the NF peaks obscures the other peaks [26], [38], [39].

XPS investigations were performed to investigate the element valence states and surface chemical states of NiCo LDH and PANI@NiCo LDH samples. In the survey spectrum of NiCo LDH (Figure 6a), presence of Co 2p, Ni 2p, C 1s (Carbon), O 1s (Oxygen), and N 1s (Nitrogen). For the PANI@NiCo LDH sample, supplementary peak sulphur is detected instigating the presence of PANI [40]. In addition, compared to NiCo LDH/NF, the Co 2p<sub>3/2</sub> and Ni 2p<sub>3/2</sub> peak shifted to higher binding energies from 780.83 to 781.38 eV for Co 2p<sub>3/2</sub> and from 855.60 to 856 eV for Ni 2p<sub>1/2</sub> and are slightly wider for PANI@NiCo LDH/NF, suggesting the introduction of PANI (Figure 6b, c). It is probable that PANI's quinone nitrogen atoms partially transmetalate with the Ni and Co nodes in NiCo LDH to coordinate with Ni and Co [38]. Because metals and metal ions can donate or accept electrons, coordination to them generally changes the binding energy [38]. Therefore, it can be concluded that electrodeposition of the PANI layer on NF influenced the formation of LDH samples.

In Ni 2p spectrum of PANI@NiCo LDH/NF (Figure 6d), two major peaks positioned at 874.12 and 856.23 eV corresponds to Ni<sup>2+</sup> and other peaks at 878.10 and 860.083 eV attributed to Ni<sup>3+</sup>, both sets allocated for Ni 2p<sub>1/2</sub> and Ni 2p<sub>3/2</sub> respectively. Two excitation shake-up satellite peaks (labelled sat.) are positioned at 881 and 863.70 eV [41]. For the Co 2p core-level spectrum (Figure 6e), the peaks at 798.42 eV and 796.60 eV are attributed to 2p<sub>1/2</sub> ascribed to Co<sup>2+</sup> and Co<sup>3+</sup> respectively. Whereas, other fitted peaks at 782.94 eV and 780.92 eV correspond to Co 2p<sub>1/2</sub> for Co<sup>2+</sup> and Co<sup>3+</sup> respectively. Additionally, pair of shakeup excitation shake-up satellite peaks positioned at 803.19 and 787.29 eV respectively [41][42]. As is shown in Figure 6f, in N 1s spectrum, peaks at 400.82, 399.2, and 407.06 eV are corresponding to nitrogen, benzenoid amine (-NH-), quinonoid amine (=N-), cationic amine (-N<sup>+</sup>-) respectively, conforming the interaction of NiCo LDH and PANI layer, helpful in providing significant enhance performance due to the rapid transfer of electron [43]. The deconvolution peak of O 1s as shown in Figure 6g is located at 533.60, 531.74 and 530.55 eV correspond to the M-O-M, M-O (M=Ni, Co), and O-H respectively. The core-level spectrum for C 1s as demonstrated in Figure 6h, display

peaks at 287.10, 286.11, and 284.86 eV attributed to carbonyl group C=O, C-N, and C=C groups respectively [37]. The XPS analysis revealed the presence of LDH and PANI layers in the PANI@NiCo LDH/NF sample, which provided numerous electroactive sites for redox processes and enhanced the material's energy storage capacity.

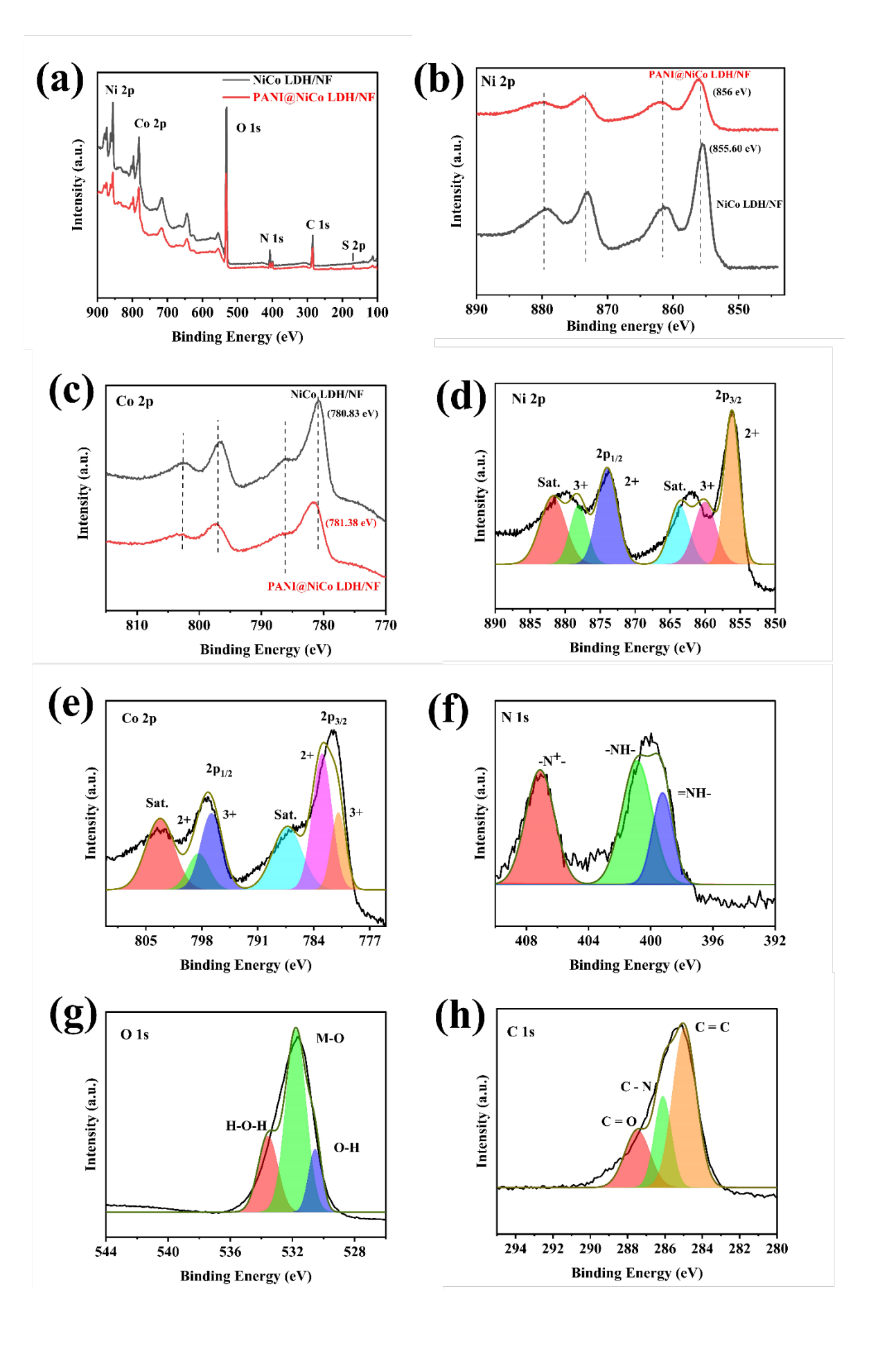


Figure 6. XPS curves (a-c). Comparative full scan survey, Comparative Ni 2p, Comparative Co 2p for NiCo LDH/NF and PANI@NiCo LDH/ NF respectively, (d-h). Ni 2p, Co 2p, N 1s, O 1s, and C 1s for sample PANI@NiCo LDH/NF

# 5. Electrochemical Investigations in Three-electrode configurations

The electrochemical properties of PANI@NiCo LDH electrode was evaluated in standard three-cell setup in a 1.0 M KOH electrolyte, with all tests conducted at room temperature. For comparison, the energy storage performance of NiCo LDH/NF, PANI/NF, and NF were also investigated using similar three-electrode cell. The comparative CV curve of aforementioned samples within the voltage window of 0-0.5 V, at a sweep rate of 2 mV/sec is demonstrated in Figure 7a. As can be observed, NF substrate have minimal specific area, implying much lower specific capacitance as compare to other capacitive material. Apparently, PANI@NiCo LDH/NF exhibits much larger CV area compared with that of NiCo-LDH/NF and PANI/NF which indicates its superior capacitance. Inevitably, after the appropriate amount of PANI layer was deposited, the NF surface turns rough. When compared to NiCo LDH, rough surfaces offer more chemical active sites, which is advantageous for enhancing electrochemical performance. Furthermore, PANI layer serves as a conductive channel for ion transport, and promotes electrolyte penetration [44]. Whereas, NiCo LDH porous and interconnected nanosheets provide narrow channels for the rapid diffusion of electrolytic ions. As a result, synergy between PANI and NiCo LDH improves the Faraday redox reaction kinetics that proves beneficial for boosting electrochemical parameters. Additionally, as seen in SEM (Figures 2(c, d), the loose 3D nanosheet topology offers increased electroactive surface area, provides more redox active sites, and an electron highway to lower interfacial resistance, all of which contribute to better energy storage performance [45].

Additionally, the CV curve of LDH samples shows a prominent, distinct peak at about 0.17 and 0.36 V, suggesting LDH's battery like behaviour and is controlled by reversible Faradic redox processes between Ni<sup>2+</sup> /Ni<sup>3+</sup>, Co<sup>2+</sup>/Co<sup>3+</sup> with OH<sup>-</sup>, as given in equation (10)-(12)

$$Co(OH)_2$$
 (Cobalt(II) hydroxide) + OH<sup>-</sup>(ion)  $\rightarrow$  CoOOH + H<sub>2</sub>O + e<sup>-</sup> (10)

$$CoOOH + OH^{-}(ion) \rightarrow CoO_2 + H_2O + e^{-}$$
(11)

$$Ni(OH)_2$$
 (Nickel(II) hydroxide) + OH<sup>-</sup> (ion)  $\rightarrow$  NiOOH + H<sub>2</sub>O + e<sup>-</sup> (12)

The electrochemically active surface area (ECSA) is one of the most significant factors that indicates the area of the electrode material that is available to the electrolyte in the charge storage/transfer mechanism. The ECSA value is found to be proportional to slope of sweep rate vs. Δj(j<sub>c</sub>-j<sub>a</sub>) curve, where j<sub>c</sub> and j<sub>a</sub> stands for cathodic and anodic peak current densities at corresponding scan rate. The value of slope (Figure 7b) for PANI/NF, LDH/NF, and PANI@NiCo LDH/NF was found to be 0.6, 0.29, and 1.0 mF/cm² respectively. The PANI@NiCo LDH/NF possess higher ECSA, further validates its higher electrochemical activity, resulting in abundant active sites needed for high electrochemical performance [46], [47].

The CV graph for PANI@NiCo LDH/NF from 2 to 15 mV/sec is depicted in Figure 7c (device safety). The shape of the CV curves is similar at varied sweep rates, indicating both fast ion mass transfer as well as high reversibility of the electrode. But, with rising sweep rate, reduction peak shifts to the lower potential values whereas oxidation peak shifts to higher potential values, because of electric polarisation and kinetic irreversibility of electrolytic ions at the

electrode's surface. Also, at low scan rates, distinct redox peaks can be observed as all the active sites participated in redox reaction. On the other hand, at high rates, the oxidation peaks gradually disappear because the active sites don't get much time to fully participate in Faradaic redox reaction [48].

The CV graph is also utilised to examined the electrochemical kinetics of samples via Dunn's power equations ((13), and (14))

$$i = kv^b \tag{13}$$

$$ln(i) = b ln(v) + ln (k)$$
 (14)

Where, v (mV/sec) is the scan speed, i is the current density (A/g), and b and k are adjustable parameters. Among them, b is a crucial parameter associated with charge storage process. For capacitor and EDLC supercapacitor, charge storage is primarily accomplished by electrostatic process, b is ideally found to be 1. Given that batteries store charge through a Faradic oxidation-reduction mechanism, the value of b in this instance is determined to be 0.5. A linear relationship between ln v and ln  $i_p$  is depicted in Figure 7d. For the cathodic and anodic peaks, the b values are 0.56 and 0.55 respectively, values are smaller to 1 and near to 0.5, signifying both diffusion-controlled and surface-controlled mechanism function concurrently on PANI@NiCo LDH/NF electrode, with diffusion-controlled technique dominating during the charge storage processes, indicating the battery-like behaviour of PANI@NiCo LDH/NF. Furthermore, the curve between peak current and scan rate is shown in Figure 7e displays remarkable linearity ( $R^2 = 0.99$ ), indicating significant penetration of OH<sup>-</sup> ions at PANI@NiCo LDH/NF electrode [49]–[51].

More explicitly, the performance of the electrode was quantitatively explained by assessing the contribution from the diffusion-controlled and surface capacitive mechanism using the power equation (15):

$$i(v) = k_1 v + k_2 v^{1/2}$$
 (15)

where  $k_2v^{1/2}$  for the diffusion-controlled current and  $k_1v$  stands for the surface capacitive current, i describes peak current density (A/g) at that particular scan rate v (mV/sec). Therefore, equation (15) was used to compute the portion of diffusion-controlled and capacitive charge storage contributions, and the resulting data are presented in Fig. 7f. The contribution ratios of battery-type current were 92, 87, 85, 83, and 78% at the scan rates of 2, 5, 7, 10, and 15 mV/sec, respectively, further validating the battery-type behaviour of the PANI@NiCo LDH/NF electrode [52].

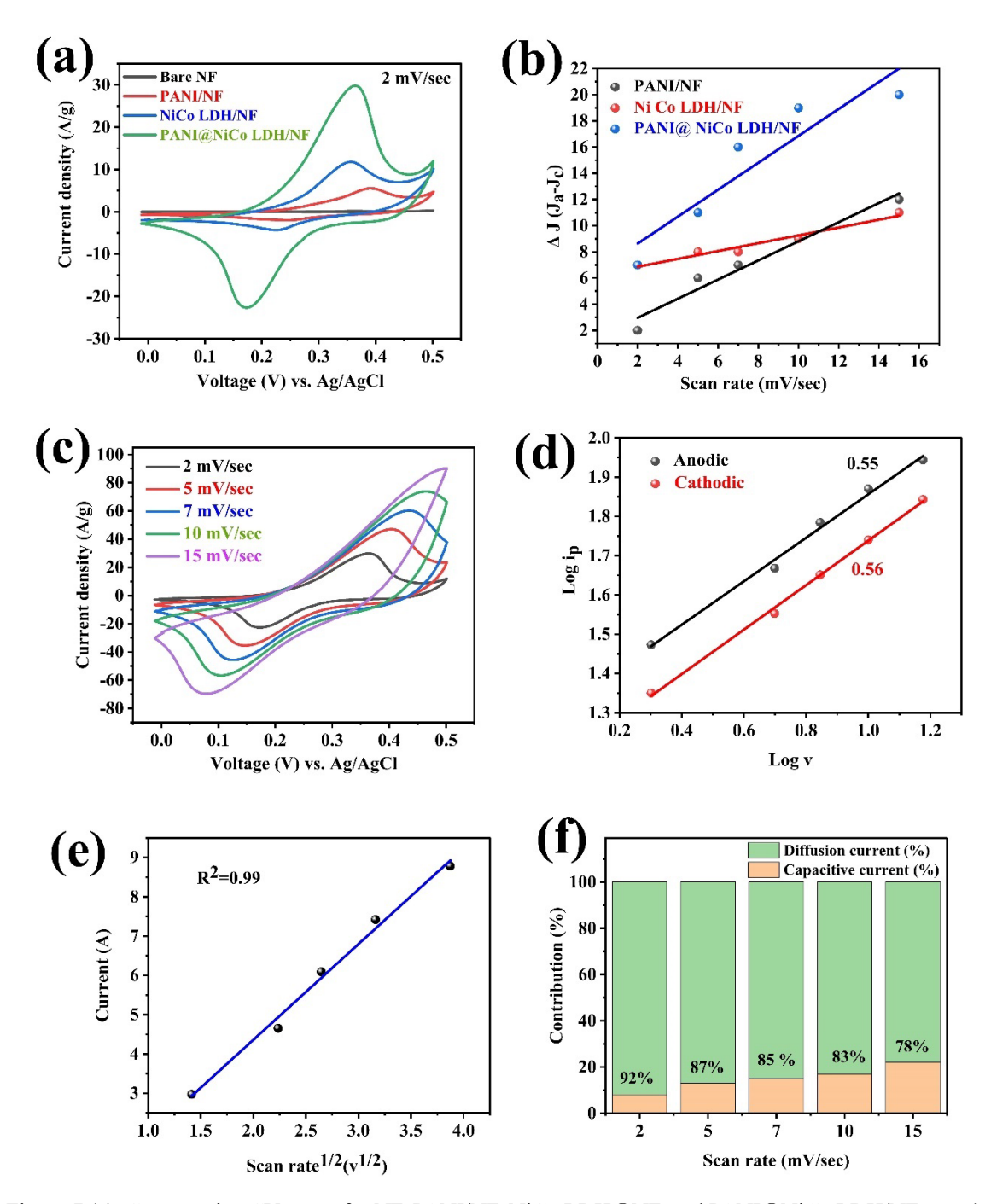


Figure 7 (a). Comparative CV curve for NF, PANI/NF, NiCo LDH@NF, and PANI@NiCo LDH/NF sample (b).  $\Delta$  J vs. scan rate curve (c) CV curve at different scan rates (d). log  $i_p$  vs. log v (e). Current vs. scan rate  $^{1/2}$  (f). current distribution curve for sample PANI@NiCo LDH/NF

The comparative GCD curve for NF, PANI/NF, NiCo LDH/NF, and PANI@ NiCo LDH/NF electrode is demonstrated in Figure 8a. Particularly, PANI@ NiCo LDH/NF show the longest discharge time among all electrodes, indicating its excellent storage capacity, well-aligned with the CV results. As calculated from equation (2), specific capacity for PANI@NiCo LDH/NF was estimated to be 1481 C/g (3703.33 F/g) which is much higher than that of NiCo LDH/NF, PANI/NF, and NF i.e., 847 C/g (2117.5 F/g), 539 C/g (1347 F/g), and 7 C/g (17.5 F/g) respectively. This is primarily attributable to nanonetwork of NiCo LDH supported on PANI, which enhances the electrode material's electrical conductivity, facilitates the passage of

electrolytic ions and electrons, and enhances the oxidation/reduction sites at electrode electrolyte interface. Also, the unique nanonetworks structure of LDH enhances the intercalation of ions within LDH's interlayer, leading to a enhance specific capacitance. Table 1 compares the specific capacitance of PANI@NiCo LDH/NF with previous published work, and it is either greater or comparable to the majority of the recent reported materials.

Table 1: Comparative specific capacity of PANI@NiCo LDH/NF with reported literature

Sample Materials	Specific capacity	Electrolyte	Voltage Window	Reference
	(C/g) (1 A/g)	(KOH)		
NiCo <sub>2</sub> O <sub>4</sub> @PANI	1243.2	6 M	0.40	[53]
PANI/NiCo-	830	2 M	0.45	[54]
LDH/CC (carbon				
cloth)				
NiCo-	901	2 M	0.45	[23]
LDH@PANI/CC				
ZnCoO <sub>x</sub> /C@PANI	422	6 M	0.40	[55]
NiCo-	$88.15 \text{ mF/cm}^2 (0.075)$	3 M	0.45	[37]
LDH/G/PANI	$mA/cm^2$ )			
PANI@NiCo <sub>2</sub> O <sub>4</sub>	720.8	0.5 M	0.80	[24]
		$H_2SO_4$		
PANI@NiCo	1481	1 M	0.40	This work
LDH/NF				

The rate capability curve i.e., specific capacity vs. current density curve for different samples is as shown in Figure 8b. It can be noted that, PANI@NiCo LDH/NF retains its specific capacitance upto 50%, even at the high current density of 30 A/g, demonstrating the electrode's quick electron transport kinetics. However, as the current density increases, there is decrease in specific capacity, might be because of the gradual shift of redox mechanism to a surface-controlled one, that ultimately causes the specific capacity to attenuate [56]. Figure 8(c, d) displays the extensive GCD graph for PANI@NiCo LDH/NF electrode, from 1 to 30 A/g current density. The symmetry and clear redox plateaus are maintained at higher current densities, that suggests high degree of redox reversibility and rapid ion transfer kinetics in PANI@NiCo LDH/NF electrode.

EIS was carried within the frequency range of 0.01 Hz to 0.1 MHz access the information related to electron transfer kinetics and ion diffusion at electrode-electrolyte interface. Comparative Nyquist curve for NF, PANI/NF, NiCo LDH/NF, and PANI@NiCo LDH/NF is depicted in Figure 8e. The equivalent circuit of the Nyquist plot is demonstrated in Figure 8(e). Nyquist plot usually features two distinct areas: a straight line in the low-frequency range and a semicircular arc in the high-frequency range. Series resistance (R<sub>s</sub>), determined by finding the intercept of the semi-circle arc with real impedance axis (Z'), attributed to the interfacial, intrinsic, electronic and diffusive resistance between the electrode-electrolyte along with the individual resistance caused by electrolyte, electrode and current collectors. The R<sub>s</sub> value for NF, PANI/NF, NiCo LDH/NF, and PANI@NiCo LDH/NF was determined as 1.4, 1.7, 2.3, and 1.8 Ohm respectively. The lower value of R<sub>s</sub> for PANI@NiCo LDH/NF electrode demonstrates that PANI layer considerably improves the conductivity, enhances electrochemical activity, and electron transfer kinetics of composite sample, well aligned with CV and GCD results. Besides, nearly vertical line (shown as "C" in equivalent circuit diagram) at low-frequency indicates the high capacitive performance with unhindered ion diffusion. Also, PANI@NiCo LDH/NF possess nearly straight vertical line compare to LDH sample, demonstrates superior capacitive

nature and rapid ion diffusion. Consequently, from three-electrode cell analysis, it can be inferred that highly conductive and porous PANI@NiCo LDH/NF electrode offers numerous active sites, enhancing its electrochemical performance, which makes it a viable candidate for supercapattery devices [57].

To assess the cycling stability of the PANI@NiCo LDH/NF electrode, a cyclability test was performed for 3000 cycles at 30 A/g. Interestingly, the electrode PANI@NiCo LDH/NF retains 98.36 % of its initial capacitance value as depicted in Figure 8f. Additionally, the coulombic efficiency ( $\eta$ ) can be calculated using equation (16) by dividing the discharge time ( $T_d$ ) by the charge time ( $T_c$ ) in GCD tests.

$$\eta = \frac{T_d}{T_c} X 100 \tag{16}$$

The coulombic efficiency was found to be 98.88% over 3000 cycles, indicating the excellent cyclic stability of the PANI@NiCo LDH/NF electrode [57].

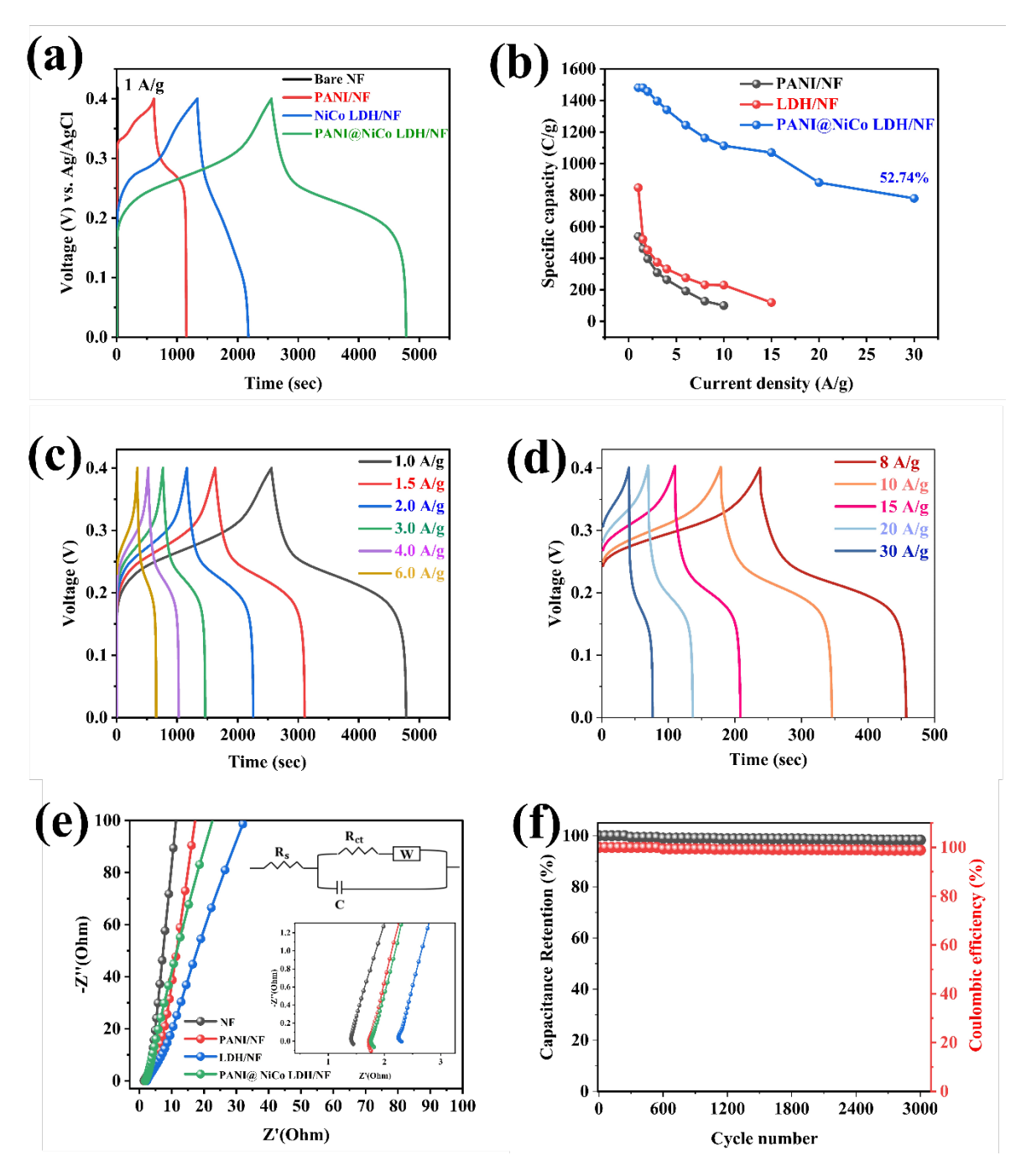


Figure 8: Comparative (a, b). GCD curve (b). Specific capacity vs. current density for PANI/NF, NiCo LDH/NF, and PANI@NiCo LDH/NF sample (c-d). GCD curve at different current density for sample PANI@NiCo LDH/NF (e.) Nyquist curve for PANI/NF, NiCo LDH/NF, and PANI@NiCo LDH/NF sample (f) Cyclic stability curve for PANI@NiCo LDH/NF sample

Thus, high electrochemical performance depicted by PANI@NiCo LDH/NF can be attributed to the following reasons: (i). the NF improves the number of active sites by acting as a highly conductive substrate while improving the electrode mechanical strength (ii). PANI layer's delocalized conjugated structure act as an intermediary for the storage and transfer of electrons. Moreover, it enhances the interaction between substrate and LDH, boosting specific capacity and offering exceptional rate capability (iii). the interlayer network of the LDH facilitates the electrolyte ions' quick insertion and extraction from the material surface, providing abundant active sites for redox process, enhancing electrochemical properties (iv). the fabrication of

LDH directly on PANI effectively decrease the interfacial resistance between the substrate and active material. As a result, this study may provide an innovative method for developing additional highly porous LDH materials based on transition metals directly on PANI that could be utilised in upcoming high-performance energy storage initiatives.

# 6. Electrochemical characterization of assembled supercapattery device: PANI@NiCo LDH//1 M KOH//rGO

A study of PANI@NiCo LDH/NF as a battery-type electrode, combined with coffee grounds derived rGO as a capacitive electrode, results in an intriguing hybrid supercappattery paradigm. This approach has immense potential to enhance the performance of energy storage devices. The two electrodes in the supercapattery device were separated by a Whatman filter paper, as illustrated in the schematic diagram of the assembled supercapattery device (Figure 9a). The movement of ions between the electrolyte and the electrode resulted in the storage of ions or charges during the conduction process. Before assembly, the electrochemical performance of rGO was evaluated in a three-cell system. Figure S3(a, b) displays the CV and GCD plot of rGO at different scan rates and current densities within the voltage range of 0-1 V. rGO exhibits a linear GCD curve and a quasi-rectangular CV curve, reflecting typical double-layer capacitive behaviour. Also, Figure S3c illustrates the Nyquist plot of rGO. The measured R<sub>s</sub> and charge transfer resistance (R<sub>ct</sub>) were found to be 1.62 Ohm and 25.38 Ohm, respectively, indicating excellent electrical conductivity. This makes it a promising choice for the anode in supercapattery devices.

The CV graph of PANI@ NiCo LDH/NF and rGO at a sweep rate of 10 mV/sec is illustrated in Figure 9b. The optimum mass ratio of PANI@ NiCo LDH/NF as anode to rGO as cathode was found to be 1:13.55, employing the mass balancing equation (3). Furthermore, the stable potential window for the rGO and PANI@ NiCo LDH/NF electrodes was determined to be −1 to 0 V and 0 to 0.5 V against Ag/AgCl, respectively. Thus, the operating voltage range of supercapattery device could be stretched near to 1.5 V. For the safety concerns, the potential range was set to 1.4 V, that ensures the two electrodes' safe operation. To better investigate the suitable operating potential range, the assembled supercapattery device was analysed with different potential range employing CV analyses (Figure S4). It is noteworthy that the supercapattery CV curves, even at high cell potential ranges (0–1.4 V), did not exhibit any obvious polarisation. Instead, they primarily demonstrated the mixed energy storage mechanisms of the assembled device, which are battery-type (caused by redox active sites that decipher PANI@ NiCo LDH/NF nanostructures) and capacitive-type (caused by surface absorption of ions rGO). As can be seen in Figure 9c, CV curves of the PANI@ NiCo LDH/NF//rGO supercapattery device at the scan rates of 5-100 mV/sec. It is important to notethat, even at higher sweep rate, shape of the CV curve remains steady along with the capacitive characteristics, demonstrates device's good reversibility and remarkable electrochemical kinetics. Additionally, the CV curve's flawed rectangular or humpy shape LDH/NF demonstrated PANI@NiCo and biomass-derived rGO, capacitive and pseudocapacitive contributions, respectively [48][58].

The GCD curves of the supercapattery device in the potential range of 0–1.4 V are demonstrated in Figure 9d. As estimated from equation (4), the specific capacitance of the device was found as 200 F/g at 1 A/g, and still retains 92 F/g at 10 A/g, suggesting its good rate capability. Furthermore, columbic efficiency remains nearly unaltered even at higher current density, demonstrating remarkable electrochemical reversibility of the assembled PANI@NiCo LDH/NF//rGO supercapattery device. Moreover, as estimated from the Nyquist plot (Figure

9f), the value of  $R_s$  was found to be 2.7 Ohm, and nearly straight line at low frequency depicted high capacitive nature of the assembled supercapattery device.

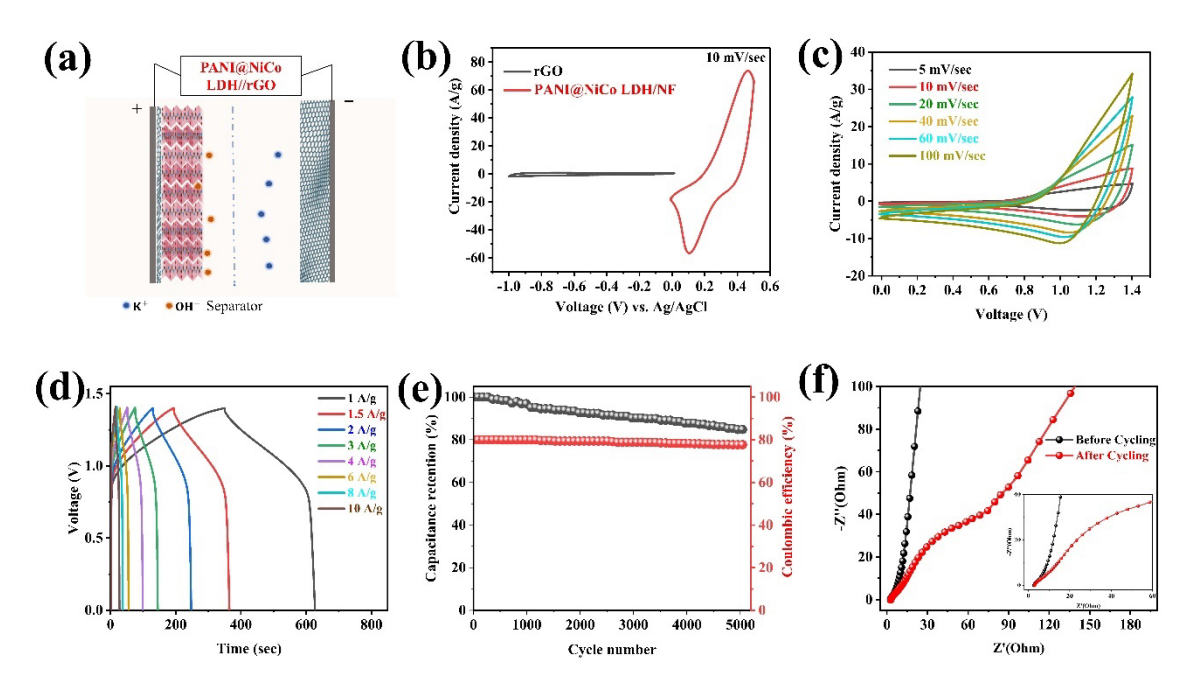


Figure 9: (a). Systemic illustration of assembled PANI@NiCo LDH/NF//rGO (b). CV curve for rGO and PANI@NiCo LDH/NF at 10 mV/sec (c, e) CV and GCD, and cyclic stability curve for PANI@NiCo LDH/NF//rGO supercapattery device (d). Nyquist curve before and after cycling of PANI@NiCo LDH/NF//rGO supercapattery device.

Further, energy density, and power density of PANI@NiCo LDH/NF//rGO supercapattery device was determined employing equation (5), and (6), which is 54.44 Wh/kg and 0.702 kW/Kg, respectively. The values are on par with or greater than the majority of other devices that have been reported, such as PANI/Ni<sub>3</sub>S<sub>2</sub>/NF-100//activated carbon (AC) (48 Wh/kg, 799 W/kg) [44], PANI/NiCo-LDH//AC (46 Wh/kg, 351 W/kg) [54], NiO-PANI// NiO-PANI (21 Wh/kg, 481 W/kg) [59], Co-Ni LDH@Co<sub>3</sub>O<sub>4</sub>@CC//carbon nanosheets (33.4 Wh/kg, 1600 NiCo-LDH@PANI@CC//AC 728 W/kg) [60],(26)Wh/kg, W/kg[23], NiCo<sub>2</sub>S<sub>4</sub>@polyaniline//Activated carbon (32 Wh/kg, 129 W/kg) [32], ZnCoOx/C-PANI-3//AC (42 Wh/kg, 705 W/kg) [55], ZnCe-MOF@PANI//AC (58 Wh/kg, 850 W/kg) [61], also demonstrated in Ragone plot (Figure 10). Furthermore, nearly 5000 charge-discharge tests at 8 A/g (Figure 9e). It's interesting to note that the estimated values for capacitance retention and Columbic efficiency are 84.88% and 77.68%, respectively over 5000 charging discharging cycles, while the value of series resistance change by small amount of  $\sim 0.2$ .

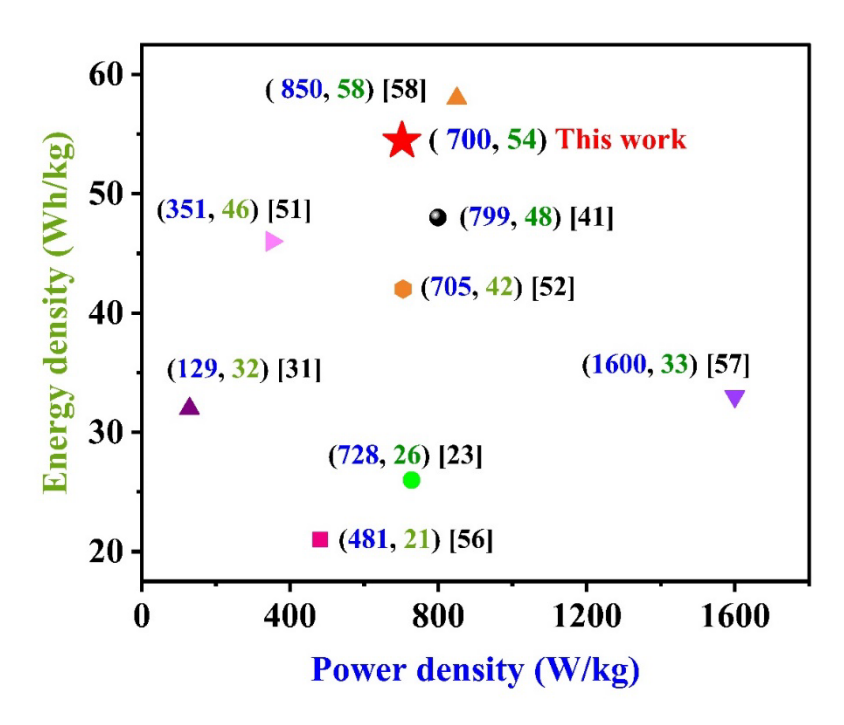


Figure 10: Ragone plot

Following cyclability testing, PANI@NiCo LDH/NF sample underwent SEM investigation, as depicted in Figure 11a. The sample's porous structure is comparable to that of the sample before cycling (Figure 2c, d), with some mild morphological changes suggesting a minor degradation in the 3D LDH morphology. Figure 11(b, c) presents the EDX patterns before and after the cyclability test, revealing a new peak of potassium, which indicates partial absorption of electrolyte on the PANI@NiCo LDH/NF electrode. The supercapattery device, with its outstanding electrochemical performance, shows significant promise as a future energy storage system. Our research notably leverages a simple method for forming well-defined internal voids in metal hydroxide frameworks on conductive network of PANI layer coupled with biomass derived rGO, so enabling their application in electrochemical processes. In addition to creating a PANI@NiCo LDH/NF electrode that is extremely efficient for use in supercapattery applications, this work highlights important sustainability benefits such using bioresources Coffee grounds, that are acquired via microwave pyrolysis and related processes. The promising findings observed in the PANI@NiCo LDH/NF//1 M KOH//rGO supercapattery, combined with material engineering and current industrious research offer possibilities for developing advanced functionalities suited for advanced handheld electronic devices.

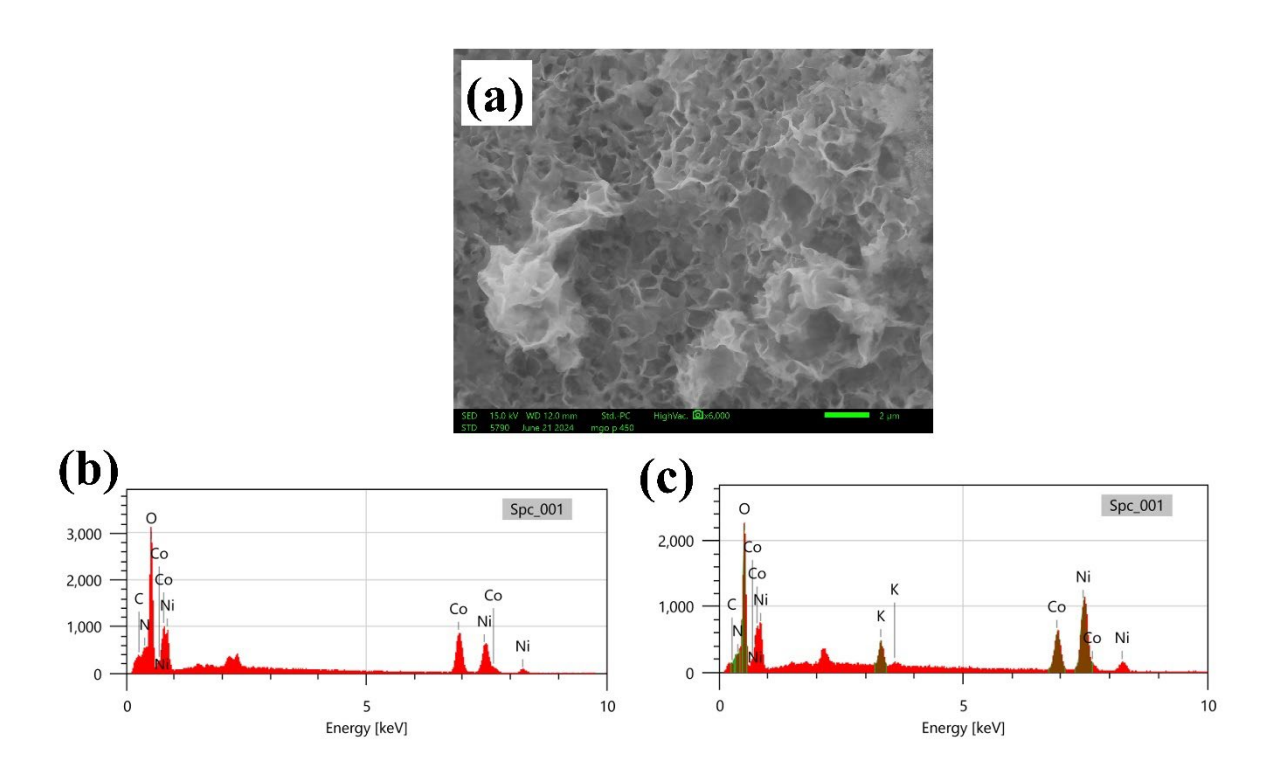


Figure 11: SEM image of PANI@NiCo LDH/NF sample after cycling test (b, c) before and after EDAX pattern of PANI@NiCo LDH/NF before and after cycling test

# **Conclusion and Future Perspectives**

When the aforementioned findings are combined together, it becomes evident that the PANI@NiCo LDH/NF device delivers remarkable performance. The findings can be explained based on the morphological, structural, and electrochemical variations demonstrated by the PANI/NF, LDH/NF, and PANI@NiCo LDH/NF sample. PANI@NiCo LDH/NF has been successfully synthesised on Nickel foam by a simple, two-step, electrodeposition and then followed with solvothermal method. The electrode's specific surface area is significantly increased by the nanosheet structure, which also offers channels for charge transit and electron storage since it contains incredibly abundant mesopores. The conductivity of NiCo LDH was enhanced by in-situ coated PANI, and the synergistic interaction between MOFs and PANI speed up the transfer of ions during charging and discharging. PANI layer serves a significant role in the composite. It promotes the growth of NiCo LDH structure, resulting in a higher mass loading on the NF substrate. As a result, specific capacitance of the PANI@NiCo LDH/NF was increased significantly to 1481 C/g (3703.33 F/g) which is much higher than that of NiCo LDH/NF, PANI/NF, and NF i.e., 847 C/g (2117.5 F/g), 539 C/g (1347 F/g), and 7 C/g (17.5 F/g) respectively. Additionally, as fabricated supercapattery device PANI@NiCo LDH/NF and rGO offer energy density of 54.44 Wh/kg at a power density of 0.702 kW/kg. Whereas, the device exhibits good cyclability with the capacitance retention and Columbic efficiency of 84.88% and 77.68%, respectively over 5000 charging discharging cycles. In order to further improve the electrochemical activity of the PANI@LDH based supercapattery device, more research is needed for the precise studies of the PANI and LDH active compounds. We believe that our work will contribute significantly to the understanding of conducting polymer hybrids and LDHs. The innovative design approach that has been provided here may also be used to directly design and fabricate different hydroxides/oxides and hybrid films of conductive polymers in order to fabricate supercapattery material with excellent electrochemical performance.

# Acknowledgement

Megha Prajapati acknowledges the financial support from IGDTUW, Delhi and JCU, Australia for her ongoing research. The authors Megha Prajapati and Chhaya Ravi Kant also express gratitude to DST, Gol, Curie Grant for providing SEM and FTIR instrument facilities at their institution. Special thanks are extended to Scarlett Allende from the Electronics Materials Lab, College of Science and Engineering, James Cook University, Townsville, for her contribution to the preparation of GO.

#### References

- [1] Z. Ye, Y. Jiang, L. Li, F. Wu, and R. Chen, *Rational Design of MOF-Based Materials for Next-Generation Rechargeable Batteries*, vol. 13, no. 1. 2021. doi: 10.1007/s40820-021-00726-z.
- [2] S. Ma *et al.*, "Temperature effect and thermal impact in lithium-ion batteries: A review," *Prog. Nat. Sci. Mater. Int.*, vol. 28, no. 6, pp. 653–666, 2018, doi: 10.1016/j.pnsc.2018.11.002.
- [3] R. Kumari, S. Kumar Sharma, V. Singh, and C. Ravi Kant, "Facile, two-step synthesis of activated carbon soot from used soybean oil and waste engine oil for supercapacitor electrodes," *Mater. Today Proc.*, vol. 67, no. xxxx, pp. 483–489, 2022, doi: 10.1016/j.matpr.2022.07.253.
- [4] R. Kumari, P. R. Kharangarh, V. Singh, R. Jha, and C. R. Kant, "Sequential processing of nitrogen-rich, biowaste-derived carbon quantum dots combined with strontium cobaltite for enhanced supercapacitive performance," *J. Alloys Compd.*, p. 172256, 2023, doi: https://doi.org/10.1016/j.jallcom.2023.172256.
- [5] R. Kumari, V. Singh, and C. Ravi, "Enhanced performance of activated carbon-based supercapacitor derived from waste soybean oil with coffee ground additives," *Mater. Chem. Phys.*, vol. 305, no. February, p. 127882, 2023, doi: 10.1016/j.matchemphys.2023.127882.
- [6] M. Prajapati, V. Singh, M. V. Jacob, and C. Ravi Kant, "Recent advancement in metalorganic frameworks and composites for high-performance supercapatteries," *Renew. Sustain. Energy Rev.*, vol. 183, no. June, p. 113509, 2023, doi: 10.1016/j.rser.2023.113509.
- [7] M. Prajapati, C. Ravi Kant, S. Allende, and M. V Jacob, "Metal organic framework derived NiCo layered double hydroxide anode aggregated with biomass derived reduced graphene oxide cathode: A hybrid device configuration for supercapattery applications," *J. Energy Storage*, vol. 73, p. 109264, 2023, doi: https://doi.org/10.1016/j.est.2023.109264.
- [8] N. Stock and S. Biswas, "Synthesis of metal-organic frameworks (MOFs): Routes to various MOF topologies, morphologies, and composites," *Chem. Rev.*, vol. 112, no. 2, pp. 933–969, 2012, doi: 10.1021/cr200304e.
- [9] D. Alezi *et al.*, "MOF Crystal Chemistry Paving the Way to Gas Storage Needs: Aluminum-Based soc-MOF for CH4, O2, and CO2 Storage," *J. Am. Chem. Soc.*, vol. 137, no. 41, pp. 13308–13318, Oct. 2015, doi: 10.1021/jacs.5b07053.
- [10] D. Kumari, M. Prajapati, and C. R. Kant, "Highly Ef fi cient Non-Enzymatic Electrochemical Glucose Biosensor Based on Copper Metal Organic Framework Coated on Graphite Sheet," *ECS J. Solid State Sci. Technol.*, vol. 13, no. 4, p. 47007, 2024, doi: 10.1149/2162-8777/ad3fe5.
- [11] Z. Luo *et al.*, "Metal–Organic Framework (MOF)-based Nanomaterials for Biomedical Applications," *Curr. Med. Chem.*, vol. 26, no. 18, pp. 3341–3369, 2018, doi:

- 10.2174/0929867325666180214123500.
- [12] R. Kumari, M. Prajapati, and C. R. Kant, "NiCo MOF @ Carbon Quantum Dots Anode with Soot Derived Activated Carbon Cathode: An Efficient Asymmetric Configuration for Sustainable High-Performance Supercapacitors," vol. 2400109, pp. 1–15, 2024, doi: 10.1002/adsu.202400109.
- [13] M. Prajapati, C. Ravi Kant, and M. V. Jacob, "Binder free cobalt Manganese layered double hydroxide anode conjugated with bioderived rGO cathode for sustainable, high-performance asymmetric supercapacitors," *J. Electroanal. Chem.*, vol. 961, no. February, p. 118242, 2024, doi: 10.1016/j.jelechem.2024.118242.
- [14] F. Luo, X. San, Y. Wang, D. Meng, and K. Tao, "Layered double hydroxide-based electrode materials derived from metal—organic frameworks: synthesis and applications in supercapacitors," *Dalt. Trans.*, vol. 53, no. 25, pp. 10403–10415, 2024, doi: 10.1039/D4DT01344A.
- [15] Q. Bi, X. Hu, and K. Tao, "MOF-derived NiCo-LDH Nanocages on CuO Nanorod Arrays for Robust and High Energy Density Asymmetric Supercapacitors," *Chem. A Eur. J.*, vol. 29, no. 11, p. e202203264, Feb. 2023, doi: https://doi.org/10.1002/chem.202203264.
- [16] M. Huang, Y. Wang, J. Chen, D. He, J. He, and Y. Wang, "Biomimetic design of Ni Co LDH composites linked by carbon nanotubes with plant conduction tissues characteristic for hybrid supercapacitors," *Electrochim. Acta*, vol. 381, p. 138289, 2021, doi: 10.1016/j.electacta.2021.138289.
- [17] F. Chen *et al.*, "Synthesis of CuO@CoNi LDH on Cu foam for high-performance supercapacitors," *Chem. Eng. J.*, vol. 401, no. March, p. 126145, 2020, doi: 10.1016/j.cej.2020.126145.
- [18] F. Cao *et al.*, "Hierarchical sheet-like Ni–Co layered double hydroxide derived from a MOF template for high-performance supercapacitors," *Synth. Met.*, vol. 234, no. November, pp. 154–160, 2017, doi: 10.1016/j.synthmet.2017.11.001.
- [19] T. Wang *et al.*, "2-Methylimidazole-Derived Ni-Co Layered Double Hydroxide Nanosheets as High Rate Capability and High Energy Density Storage Material in Hybrid Supercapacitors," *ACS Appl. Mater. Interfaces*, vol. 9, no. 18, pp. 15510–15524, 2017, doi: 10.1021/acsami.7b02987.
- [20] X. Liu, L. Zhang, X. Gao, C. Guan, Y. Hu, and J. Wang, "Enlarged Interlayer Spacing in Cobalt-Manganese Layered Double Hydroxide Guiding Transformation to Layered Structure for High Supercapacitance," *ACS Appl. Mater. Interfaces*, vol. 11, no. 26, pp. 23236–23243, 2019, doi: 10.1021/acsami.9b05564.
- [21] J. Shi, H. Tai, D. Xu, X. Kang, and Z. Liu, "Efficient improvement in the electrochemical performance of petal-like lamellar NiMn–LDHs with affluent oxygen vacancies derived from Mn MOF-74," *Dalt. Trans.*, vol. 53, no. 7, pp. 3167–3179, 2024, doi: 10.1039/D3DT03807F.
- [22] H. Zhu, S. Peng, and W. Jiang, "Electrochemical properties of PANI as single electrode of electrochemical capacitors in acid electrolytes," *Sci. World J.*, vol. 2013, 2013, doi: 10.1155/2013/940153.
- [23] W. Hu, L. Chen, M. Du, Y. Song, Z. Wu, and Q. Zheng, "Hierarchical NiCo-layered double hydroxide nanoscroll@PANI nanocomposite for high performance battery-type supercapacitor," *Electrochim. Acta*, vol. 338, p. 135869, 2020, doi: 10.1016/j.electacta.2020.135869.
- [24] C. Pan, Z. Liu, W. Li, Y. Zhuang, Q. Wang, and S. Chen, "NiCo2O4@Polyaniline Nanotubes Heterostructure Anchored on Carbon Textiles with Enhanced Electrochemical Performance for Supercapacitor Application," *J. Phys. Chem. C*, vol. 123, no. 42, pp. 25549–25558, 2019, doi: 10.1021/acs.jpcc.9b06070.

- [25] F. Fenniche, Y. Khane, A. Henni, D. Aouf, and D. Elhak Djafri, "Synthesis and characterization of PANI nanofibers high-performance thin films via electrochemical methods," *Results Chem.*, vol. 4, no. October, p. 100596, 2022, doi: 10.1016/j.rechem.2022.100596.
- [26] H. Zhang, J. Wang, Z. Wang, F. Zhang, and S. Wang, "Electrodeposition of polyaniline nanostructures: A lamellar structure," *Synth. Met.*, vol. 159, no. 3–4, pp. 277–281, 2009, doi: 10.1016/j.synthmet.2008.09.015.
- [27] S. Rami, "Synthesis, Characterization, and Electrochemical Properties of Polyaniline Thin Films," *J. Macromol. Sci. Part A Chem.*, 2015, [Online]. Available: http://scholarcommons.usf.edu/etd/5563
- [28] F. Li, Z. Sun, H. Jiang, Z. Ma, Q. Wang, and F. Qu, "Ion-Exchange Synthesis of Ternary FeCoNi-Layered Double Hydroxide Nanocage Toward Enhanced Oxygen Evolution Reaction and Supercapacitor," *Energy and Fuels*, vol. 34, no. 9, pp. 11628–11636, 2020, doi: 10.1021/acs.energyfuels.0c02533.
- [29] B. Wang, J. Tang, and F. Wang, "Electrochemical polymerization of aniline," *Synth. Met.*, vol. 18, no. 1–3, pp. 323–328, 1987, doi: 10.1016/0379-6779(87)90899-X.
- [30] M. U. Tahir *et al.*, "Room temperature and aqueous synthesis of bimetallic ZIF derived CoNi layered double hydroxides and their applications in asymmetric supercapacitors," *J. Colloid Interface Sci.*, vol. 579, pp. 195–204, 2020, doi: 10.1016/j.jcis.2020.06.050.
- [31] S. Meng, Y. Wang, Y. Zhang, Q. Xu, D. Jiang, and M. Chen, "Designing positive electrodes based on 3D hierarchical CoMn2O4@NiMn-LDH nanoarray composites for high energy and power density supercapacitors," *CrystEngComm*, vol. 22, no. 41, pp. 6864–6875, 2020, doi: 10.1039/d0ce01131b.
- [32] X. Huang and L. Gou, "High performance asymmetric supercapacitor based on hierarchical flower-like NiCo2S4@polyaniline," *Appl. Surf. Sci.*, vol. 487, no. December 2018, pp. 68–76, 2019, doi: 10.1016/j.apsusc.2019.05.005.
- [33] S. Liu *et al.*, "Hierarchical MnCo-layered double hydroxides@Ni(OH)2 core-shell heterostructures as advanced electrodes for supercapacitors," *J. Mater. Chem. A*, vol. 5, no. 3, pp. 1043–1049, 2017, doi: 10.1039/c6ta07842g.
- [34] H. Wang, Q. He, F. Zhan, and L. Chen, "Fe, Co-codoped layered double hydroxide nanosheet arrays derived from zeolitic imidazolate frameworks for high-performance aqueous hybrid supercapacitors and Zn-Ni batteries," *J. Colloid Interface Sci.*, vol. 630, pp. 286–296, 2023, doi: 10.1016/j.jcis.2022.09.092.
- [35] H. Chen, L. Hu, M. Chen, Y. Yan, and L. Wu, "Nickel Cobalt Layered Double Hydroxide Nanosheets for High-performance Supercapacitor Electrode Materials," 2013, doi: 10.1002/adfm.201301747.
- [36] R. Kumari, M. Prajapati, and C. R. Kant, "X Ray Irradiation Induced Enhancement of Supercapacitive Properties of Bio derived Activated Carbon," *J. Electron. Mater.*, no. 0123456789, 2024, doi: 10.1007/s11664-024-11048-2.
- [37] S. Ramandi and M. H. Entezari, "Self-supporting electrode for flexible supercapacitors: NiCo-layered double hydroxide derived from metal organic frameworks wrapped on graphene/polyaniline nanotubes@cotton cloth," *J. Energy Storage*, vol. 56, no. PB, p. 106106, 2022, doi: 10.1016/j.est.2022.106106.
- [38] A. P. M. Udayan, O. Sadak, and S. Gunasekaran, "Metal-Organic Framework/Polyaniline Nanocomposites for Lightweight Energy Storage," *ACS Appl. Energy Mater.*, vol. 3, no. 12, pp. 12368–12377, 2020, doi: 10.1021/acsaem.0c02376.
- [39] A. Sayah, F. Habelhames, A. Bahloul, and A. Boudjadi, "The effect of electrodeposition applied potential on the electrochemical performance of polyaniline films," *J. Mater. Sci. Mater. Electron.*, vol. 32, no. 8, pp. 10692–10701, 2021, doi:

- 10.1007/s10854-021-05725-9.
- [40] G. Yang, T. Takei, S. Yanagida, and N. Kumada, "Enhanced supercapacitor performance based on coal layered double hydroxide-polyaniline hybrid electrodes manufactured using hydrothermal-electrodeposition technology," *Molecules*, vol. 24, no. 5, 2019, doi: 10.3390/molecules24050976.
- [41] H. Bagheri, H. Javanmardi, A. Abbasi, and S. Banihashemi, "A metal organic framework-polyaniline nanocomposite as a fiber coating for solid phase microextraction," *J. Chromatogr. A*, vol. 1431, pp. 27–35, 2016, doi: 10.1016/j.chroma.2015.12.077.
- [42] Z. Zhang, L. Han, and K. Tao, "MnOx-decorated MOF-derived nickel-cobalt bimetallic phosphide nanosheet arrays for overall water splitting," *Dalt. Trans.*, vol. 53, no. 4, pp. 1757–1765, 2023, doi: 10.1039/d3dt03631f.
- [43] C. Maddi *et al.*, "Nano-Architecture of nitrogen-doped graphene films synthesized from a solid CN source," *Sci. Rep.*, vol. 8, no. 1, 2018, doi: 10.1038/s41598-018-21639-9.
- [44] Q. Cheng, C. Yang, L. Han, and K. Tao, "Construction of Hierarchical 2D PANI/Ni3S2 Nanosheet Arrays on Ni Foam for High-Performance Asymmetric Supercapacitors," *Batter. Supercaps*, vol. 3, no. 4, pp. 370–375, Apr. 2020, doi: https://doi.org/10.1002/batt.201900221.
- [45] G. Nagaraju, S. C. Sekhar, B. Ramulu, S. K. Hussain, D. Narsimulu, and J. S. Yu, "Ternary MOF-Based Redox Active Sites Enabled 3D-on-2D Nanoarchitectured Battery-Type Electrodes for High-Energy-Density Supercapatteries," *Nano-Micro Lett.*, vol. 13, no. 1, pp. 1–18, 2021, doi: 10.1007/s40820-020-00528-9.
- [46] M. M. Rajpure, H. S. Jadhav, and H. Kim, "Advanced LDH-MOF derived bimetallic NiCoP electrocatalyst for methanol oxidation reaction," *Colloids Surfaces A Physicochem. Eng. Asp.*, vol. 654, no. June, p. 130062, 2022, doi: 10.1016/j.colsurfa.2022.130062.
- [47] M. M. Rajpure, H. A. Bandal, H. S. Jadhav, and H. Kim, "Systematic development of bimetallic MOF and its phosphide derivative as an efficient multifunctional electrocatalyst for urea-assisted water splitting in alkaline medium," *J. Electroanal. Chem.*, vol. 923, no. September, p. 116825, 2022, doi: 10.1016/j.jelechem.2022.116825.
- [48] M. Z. Iqbal, M. M. Faisal, and S. R. A. Meshal Alzaid, "A facile approach to investigate the charge storage mechanism of MOF/PANI based supercapattery devices," *Solid State Ionics*, vol. 354, no. June, p. 115411, 2020, doi: 10.1016/j.ssi.2020.115411.
- [49] H. Wu and J. He, "Self-assembled MOF derived Co@C/rGO as positive electrode material for a supercapattery with high energy density," *Diam. Relat. Mater.*, vol. 123, no. February, p. 108912, 2022, doi: 10.1016/j.diamond.2022.108912.
- [50] T. K. Ghosh, D. L. Singh, V. Mishra, M. K. Sahoo, and G. R. Rao, "Synthesis of Nico-Ldh Using Zif-67 Nanoflake Precursor in Combination with Reduced Graphene Oxide (Rgo) for High Performance Supercapattery Application," *SSRN Electron. J.*, vol. 1, pp. 1–39, 2022, doi: 10.2139/ssrn.4039688.
- [51] M. Moradi, M. Mousavi, M. Pooriraj, M. Babamoradi, and S. Hajati, "Enhanced pseudocapacitive performance of two-dimensional Zn-metal organic framework through a post-synthetic amine functionalization," *Thin Solid Films*, vol. 749, no. March, p. 139187, 2022, doi: 10.1016/j.tsf.2022.139187.
- [52] J. J. Zhou *et al.*, "Controllable transformation of CoNi-MOF-74 on Ni foam into hierarchical-porous Co(OH)2/Ni(OH)2 micro-rods with ultra-high specific surface area for energy storage," *Chem. Eng. J.*, vol. 428, no. August 2021, pp. 1–9, 2022, doi:

- 10.1016/j.cej.2021.132123.
- [53] Y. Li *et al.*, "Facile synthesis of a Ni-based NiCo2O4-PANI composite for ultrahigh specific capacitance," *Appl. Surf. Sci.*, vol. 506, p. 144646, 2020, doi: 10.1016/j.apsusc.2019.144646.
- [54] X. Ge, Y. He, T. Plachy, N. Kazantseva, P. Saha, and Q. Cheng, "Hierarchical PANI/NiCo-LDH core-shell composite networks on carbon cloth for high performance asymmetric supercapacitor," *Nanomaterials*, vol. 9, no. 4, 2019, doi: 10.3390/nano9040527.
- [55] B. Zhou, Z. Li, D. Qin, Q. Zhang, M. Yu, and C. Yang, "Construction of tunable ZnCoOx/C-PANI electrode materials for high-performance supercapacitors," *J. Alloys Compd.*, vol. 956, p. 170327, 2023, doi: 10.1016/j.jallcom.2023.170327.
- [56] K. Karuppasamy *et al.*, "Unveiling the Redox Electrochemistry of MOF-Derived fcc-NiCo@GC Polyhedron as an Advanced Electrode Material for Boosting Specific Energy of the Supercapattery," *Small*, vol. 18, no. 14, 2022, doi: 10.1002/smll.202107284.
- [57] Y. Li *et al.*, "Zeolitic imidazolate framework-L-assisted synthesis of inorganic and organic anion-intercalated hetero-trimetallic layered double hydroxide sheets as advanced electrode materials for aqueous asymmetric super-capacitor battery," *J. Power Sources*, vol. 527, no. February, p. 231149, 2022, doi: 10.1016/j.jpowsour.2022.231149.
- [58] V. Ramasubbu, F. S. Omar, K. Ramesh, S. Ramesh, and X. S. Shajan, "Three-dimensional hierarchical nanostructured porous TiO2 aerogel/Cobalt based metalorganic framework (MOF) composite as an electrode material for supercapattery," *J. Energy Storage*, vol. 32, no. March, p. 101750, 2020, doi: 10.1016/j.est.2020.101750.
- [59] S. A. Razali and S. R. Majid, "Electrochemical performance of binder-free NiO-PANI on etched carbon cloth as active electrode material for supercapacitor," *Mater. Des.*, vol. 153, pp. 24–35, 2018, doi: 10.1016/j.matdes.2018.04.074.
- [60] D. Wang, L. Tian, D. Li, Y. Xu, and Q. Wei, "Rational design of Co–Ni layered double hydroxides electrodeposited on Co3O4 nanoneedles derived from 2D metalorganic frameworks for high-performance asymmetric supercapacitors," *J. Electroanal. Chem.*, vol. 873, p. 114377, 2020, doi: 10.1016/j.jelechem.2020.114377.
- [61] P. P. Sun, Y. H. Zhang, H. Shi, and F. N. Shi, "Controllable one step electrochemical synthesis of PANI encapsulating 3d-4f bimetal MOFs heterostructures as electrode materials for high-performance supercapacitors," *Chem. Eng. J.*, vol. 427, p. 130836, 2022, doi: 10.1016/j.cej.2021.130836.